PNAS RESEARCH ARTICLE | CHEMISTRY

Constructing molecule-metal relay catalysis over heterophase metallene for high-performance rechargeable zinc-nitrate/ethanol batteries

Jingwen Zhou[a,b,c,1], Yuecheng Xiong[a,b,1], Mingzi Sun[d,1], Zhihang Xu[e,1], Yunhao Wang[a,1], Pengyi Lu[a,b], Fu Liu[a], Fengkun Hao[a], Tianyi Feng[a], Yangbo Ma[a], Jinwen Yin[a], Chenliang Ye[f], Biao Chen[g], Shibo Xi[h,2], Ye Zhu[e,2], Bolong Huang[d,2], and Zhanxi Fan[a,b,i,2]

Edited by Alexis Bell, University of California, Berkeley, CA; received July 1, 2023; accepted October 26, 2023

Zinc-nitrate batteries can integrate energy supply, ammonia electrosynthesis, and sewage disposal into one electrochemical device. However, current zinc-nitrate batteries still severely suffer from the limited energy density and poor rechargeability. Here, we report the synthesis of tetraphenylporphyrin (tpp)-modified heterophase (amorphous/crystalline) rhodium-copper alloy metallenes (RhCu M-tpp). Using RhCu M-tpp as a bifunctional catalyst for nitrate reduction reaction (NO_3RR) and ethanol oxidation reaction in neutral solution, a highly rechargeable and low-overpotential zinc-nitrate/ethanol battery is successfully constructed, which exhibits outstanding energy density of 117364.6 Wh kg^{-1}_{cat}, superior rate capability, excellent cycling stability of ~400 cycles, and potential ammonium acetate production. Ex/in situ experimental studies and theoretical calculations reveal that there is a molecule-metal relay catalysis in NO_3RR over RhCu M-tpp that significantly facilitates the ammonia selectivity and reaction kinetics via a low energy barrier pathway. This work provides an effective design strategy of multifunctional metal-based catalysts toward the high-performance zinc-based hybrid energy systems.

two-dimensional materials | metallene | relay catalysis | electrocatalytic nitrate reduction | zinc-nitrate/ethanol batteries

Significance

Zinc-nitrate batteries have been regarded as a competitive candidate for next-generation power accessories, which integrate energy supply, ammonia electrosynthesis, and sewage disposal into one electrochemical device. However, previous zinc-nitrate batteries are facing challenges of low energy density and unsatisfactory rechargeability. Here, the tetraphenylporphyrin (tpp) modified heterophase (amorphous/crystalline) rhodium-copper alloy metallene (RhCu M-tpp) is synthesized as a bifunctional catalyst to enable low-overpotential nitrate reduction and ethanol oxidation reaction in neutral medium. Given the excellent performance of RhCu M-tpp, a rechargeable zinc-nitrate/ethanol battery with high energy density has been constructed. Experimental and simulation studies suggest there exists a molecule-metal relay catalytic mechanism in nitrate reduction over RhCu M-tpp, which significantly facilitates reaction kinetics and selectivity via a low energy barrier pathway.

Ammonia (NH_3) and its derivatives like fertilizers are of great significance for the sustainable development of earth's biosphere containing humankind, animals, plants, and microorganisms (1–3). The current artificial production of NH_3 heavily relies on the industrial Haber–Bosch process, which proceeds under harsh conditions (e.g., temperature: 450-500 °C, pressure: 200 atm) and shows a limited conversion percentage of 10–20% because of the extremely stable and non-polar N ≡ N bonds (941 kJ mol^{-1}) (4–6). Therefore, developing alternative and efficient synthetic technologies for the conversion of abundant N-containing species to NH_3 has become an urgent and important task on the way to achieving carbon neutral and sustainable global nitrogen cycling (7–13).

Among different strategies for NH_3 synthesis, electrocatalytic nitrate reduction reaction (NO_3RR) is regarded as a promising approach to produce NH_3 in a high yield rate, owing to the relatively low bond energy (204 kJ mol^{-1}) of N = O and good solubility of nitrate (NO_3^-) (14–16). Compared with the electrochemical N_2 reduction reaction that faces the similar issues on N ≡ N cleavage, these favorable features make NO_3RR more accessible to industrial-level production and even more feasible to be extended to civil facilities and equipment through interdisciplinary technology hybridization (17–19). In light of this, as a representative, zinc-nitrate (Zn-NO_3^-) batteries possessing a high theoretical energy density of 1,051 Wh kg^{-1} can be established after coupling NO_3RR (cathodic reaction) with a redox pair of Zn^{2+}/Zn (anodic reaction) ($E^{\theta}(Zn^{2+}/Zn) = -1.27\ V$ (vs. standard hydrogen electrode (SHE), via $Zn + 2OH^- \rightleftharpoons ZnO + H_2O + 2e^-$) (20, 21). Such self-powered metal-NO_3^- battery is a successful demonstration of "killing three birds with one stone" strategy combining energy supply, NH_3 electrosynthesis and sewage disposal (e.g., removing NO_3^--based pollutants), which enables it very attractive for the development of next-generation, high-performance, and eco-friendly power sources toward distributed stationary energy storage and electric vehicles (5, 22, 23).

According to the general working principles, the NO_3RR activity of cathode catalysts is a key factor that determines the electrochemical performance of assembled Zn-NO_3^- batteries (24–26). Among reported metal-based species for NO_3RR, copper (Cu) has been regarded as one of the most effective elements that can electrochemically convert NO_3^- into NH_3 with relatively good Faradaic efficiencies (FEs) (27–30). Nevertheless, on the one hand, most of the Cu-based catalysts exhibit the best performance for NO_3RR at quite negative applied potentials [approximately −0.4 to −0.7 V (vs. reversible hydrogen electrode (RHE)] in alkaline solutions, while more negative around −0.6 to −1.2 V (vs. RHE) in

[1]J.Z., Y.X., M.S., Z.X., and Y.W. contributed equally to this work.

[2]To whom correspondence may be addressed. Email: xi_shibo@isce2.a-star.edu.sg, yezhu@polyu.edu.hk, bhuang@polyu.edu.hk, or zhanxi.fan@cityu.edu.hk.

This article contains supporting information online at https://www.pnas.org/lookup/suppl/doi:10.1073/pnas.2311149120/-/DCSupplemental.

Published December 8, 2023.

neutral solutions) due to the weak adsorption of Cu toward protons (2, 31, 32). As a result, it requires a large overpotential to enrich proton coverage on Cu surfaces and overcome a large energy barrier of hydrogenation, which decreases the equilibrium potential gaps (i.e., working voltages of Zn-NO_3^- batteries) between cathodic NO_3^-/NH_3 and anodic Zn^{2+}/Zn pairs (20, 33, 34). This is particularly the case when assembled batteries are discharging at high rates. On the other hand, the ammonia yield rates are far away from satisfactory because of the very limited atomic utilization efficiency of large-sized Cu agglomerates, causing a severe limitation on the mass-specific capacity of cathode catalysts (35–37). Owing to these issues, the practical energy density of assembled Zn-NO_3^- batteries is suppressed heavily. Despite nanostructure modulation and atomic dispersion strategies can offset the deficiencies of Cu-based catalysts to some extent, it seems to exist a trade-off relationship between the applied potentials and ammonia FEs at the NO_3RR cathodic side so far (32, 38). Thus, how to realize sufficient FEs of NH_3 within the low-overpotential range [e.g., potential > −0.4 V (vs. RHE)] still remains a great challenge, especially in the neutral electrolytes.

Another crucial technical hurdle facing Zn-NO_3^- batteries lies in their poor rechargeability (20, 29, 34). Due to the monofunctional design of most previous catalysts for NO_3RR, their assembled Zn-NO_3^- batteries commonly worked as the galvanic cells at the sacrifice of Zn plates. Refreshing anodic electrolytes and Zn anodes from encapsulated battery devices involves another complex production line which requires great energy investment and tedious operation. Such a feature is detrimental to the deployment of Zn-NO_3^- batteries toward grid-level energy storage or electric transportation facilities, which has been frequently neglected (33, 39). To overcome this weakness, oxygen evolution reaction (OER) at the cathodic side has been attempted to offer electrons for zinc deposition on the anode. However, most catalysts with good electrocatalytic activity toward NO_3RR are not suitable and stable for OER, making the batteries non-rechargeable or have a large charge plateau and quite limited cycling life (40, 41). Meanwhile, it is not energy economical if the only beneficial point of OER is recharging the battery, and there could be several potential safety hazards like high pressure, fire, and explosion in sealed power units due to the generated O_2 gas. Unfortunately, there still lack effective bifunctional catalysts and electrochemical systems to construct high-performance, rechargeable, and eco-friendly Zn-NO_3^- hybrid energy conversion and storage devices.

In this work, a molecule-metal relay catalysis strategy is proposed to promote the conversion of NO_3^- to NH_3 at low overpotentials in neutral solution using tetraphenylporphyrin (tpp)-modified heterophase (amorphous/crystalline) rhodium-copper alloy metallene (RhCu M-tpp). Notably, RhCu M-tpp demonstrates excellent ammonia FEs over the potential window of −0.1 to −0.4 V (vs. RHE) and the highest ammonia FE of 84.8% at −0.2 V (vs. RHE) in neutral medium, much better than the Cu, Rh, and RhCu counterparts. Moreover, ethanol (EtOH) is introduced into the NO_3RR electrolyte to replace OER with ethanol oxidation reaction (EOR) in order to boost the energy economy during charging. The constructed Zn-nitrate/ethanol battery is rechargeable and delivers an outstanding energy density of 117364.6 Wh kg^{-1}_{cat}, superior rate capability, and excellent cycling stability of ~400 cycles. Ammonium acetate (CH_3COONH_4), which is widely used in chemical analysis, food industry, and pharmaceutical development, can be formed in the recycled electrolyte after long-term use of batteries. Experimental investigations and density functional theory (DFT) calculations have demonstrated that the electroactivity of interfaces between crystalline and amorphous RhCu is further activated by the introduction of tpp, offering more diverse active sites for nitrate reduction. The surface tpp plays as the initial active site for NO_3^- reduction to NO_2^- while the subsequent reduction is accelerated by the interface regions, which collectively contribute to the efficient electrocatalysis.

Results

Synthesis and Characterization. The synthesis of RhCu M-tpp is schematically illustrated in Fig. 1*A* (see more details in *SI Appendix*, Methods). Generally, through a homogeneous nucleation and slow growth process where iodide ions acted as both complexing and capping agents to induce the formation of two-dimensional (2D) nanostructures rather than zero-dimensional (0D) ones, ultrathin RhCu alloy metallene (RhCu M) was synthesized in the first step. After that, RhCu M-tpp was obtained by a facile ligand exchange approach given the strong interaction between Cu atoms in RhCu M and N atoms in tpp molecules.

X-ray diffraction (XRD) demonstrates that RhCu M exists as face-centered cubic (fcc) alloy (Fig. 1*B*) (42, 43). After the tpp surface modification of RhCu M, RhCu M-tpp was prepared, without recognizable structure change (Fig. 1*B*). The weak and broad diffraction peaks also suggest their low-crystalline and ultrathin characteristics. Scanning electron microscopy (SEM) image shows that RhCu M-tpp appears like a micrometer-sized self-assembly network where 2D ultrathin flexible RhCu M-tpp nanosheets are interconnected and wrinkles are easily observed on their surface (Fig. 1*C*), quite similar to that of graphene. Energy-dispersive X-ray spectroscopy (EDS) reveals that the corresponding Rh/Cu atomic ratio is nearly 77/23 (*SI Appendix*, Fig. S1). The above observation is similar to that of RhCu M (*SI Appendix*, Figs. S2 and S3), indicating that tpp modification has neglectable influence on the morphology and composition of RhCu metallene.

The detailed microstructures were investigated by transmission electron microscopy (TEM) and aberration-corrected high-angle annular dark-field scanning TEM (HAADF-STEM). As shown in Fig. 1*D*, the quite low contrast between nanosheets and carbon support suggests the few-layer nature of RhCu M-tpp. The lateral size of nanosheets lies in hundreds of nanometers while the thickness is below 1 nm, giving rise to abundant low-coordination active sites exposed on the surface. Electron energy loss spectroscopy (EELS) revealed that RhCu M-tpp demonstrates a sharp increase in N signal and a discernible near-edge fine structure of C-K when compared to RhCu M (Fig. 1*E*). These characteristic signals arise from the tpp molecules on the surface of RhCu M-tpp, which differ from the C signal detected in RhCu M from the carbon coating in the Cu grid and the N signal from oleylamine. These observations confirmed the presence of tpp molecules on the surface of RhCu M-tpp, which was further proved by the Fourier transform infrared spectroscopy (FT-IR) (*SI Appendix*, Fig. S4). Besides, the low-magnification and low-dose high-resolution HAADF-STEM images show that the in-plane 2D alloy structure is rich of pits and holes (with a diameter of 2–5 nm) (*SI Appendix*, Fig. S5). Note that a low-dose imaging mode was adopted to exclude the e-beam damage effect. Interestingly, crystalline domains coexist with amorphous domains in RhCu M-tpp, resulting in a crystalline/amorphous heterophase structure (Fig. 1 *F* and *I* and *SI Appendix*, Fig. S6), which is further identified by the selected-area fast Fourier transform (FFT) patterns (Fig. 1 *G* and *H*). The HAADF-STEM image and corresponding EDS elemental mappings display the uniform distribution of Rh, Cu, and N (Fig. 1 *J*–*M*). It should be noted that similar pits and holes along with amorphous/crystalline domains are also observed in the pristine RhCu M and Rh M (*SI Appendix*, Figs. S7 and S8).

The electronic structure and coordination environment of as-obtained metallenes were further studied with X-ray absorption near-edge structure (XANES) and extended X-ray absorption fine

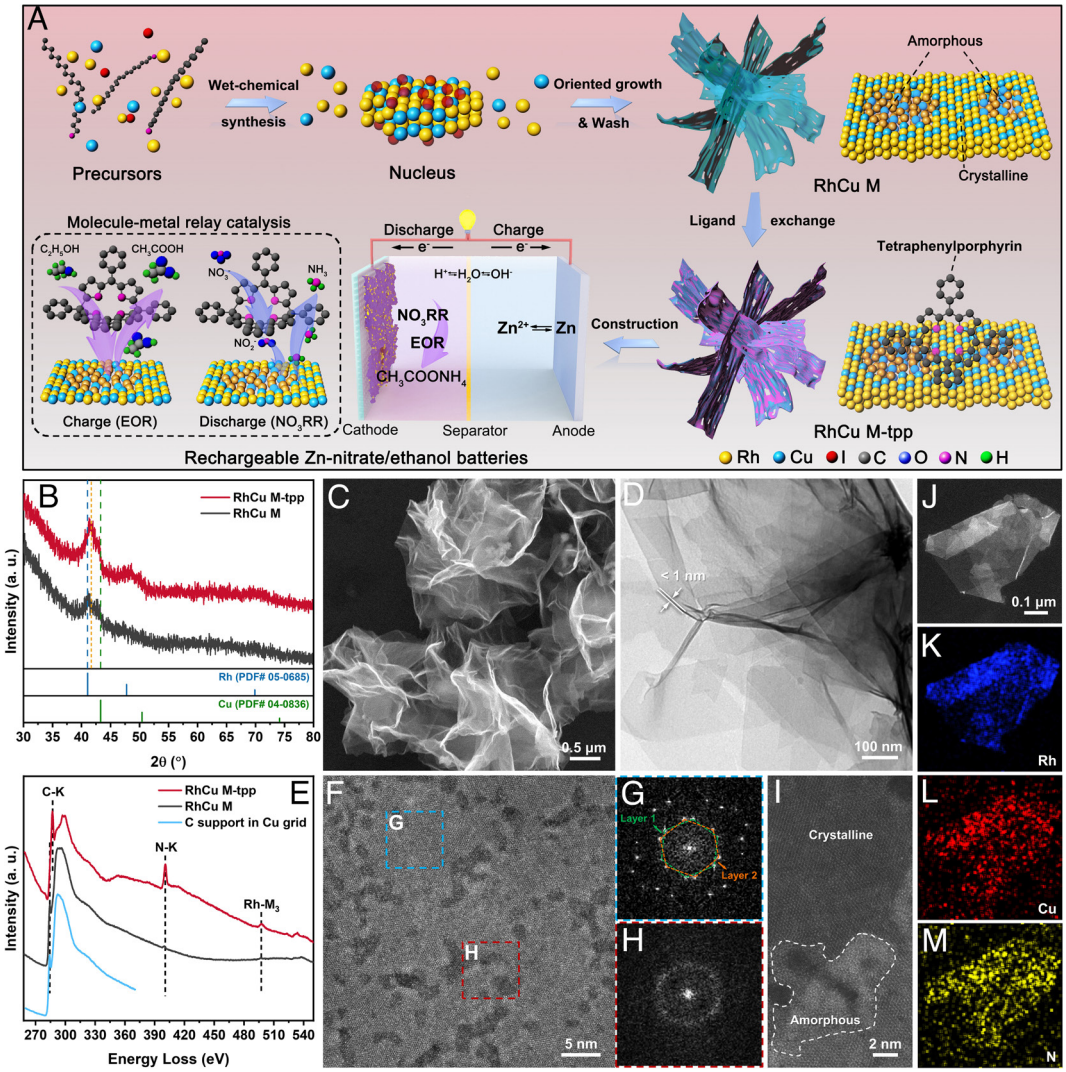

Fig. 1. Synthesis and structural characterizations. (*A*) Schematic illustration for the synthetic procedure of RhCu M-tpp and the working principle of assembled Zn-nitrate/ethanol batteries. (*B–D*) XRD pattern (*B*), SEM image (*C*), and TEM image (*D*) of as-synthesized RhCu M-tpp. (*E*) EELS spectra of RhCu M-tpp, RhCu M, and carbon support in Cu grid. (*F–H*) Low-dose HAADF-STEM image taken at 1 Pa showing the crystalline and amorphous domains within RhCu M-tpp in-plane structures (*F*) and the selected-area FFT patterns (*G* and *H*) ascribed to the regions marked by the blue (*G*) and red (*H*) dashed squares in (*F*). (*I*) Zoom-in HAADF-STEM image showing the crystalline and amorphous domains. (*J–M*) HAADF-STEM image (*J*) and the corresponding elemental mappings of Rh (*K*), Cu (*L*), and N (*M*) of the RhCu M-tpp.

structure (EXAFS) spectroscopies. As shown in Fig. 2*A*, the XANES spectra of RhCu M-tpp and RhCu M are similar in Cu K-edge, and their white line positions lie in the middle of those of Cu foil/Cu_2O and CuO, suggesting that Cu atoms act as an electron donor in both alloy metallenes due to the weak electronegativity (2, 38, 44, 45). In contrast, the synthesized Cu nanoparticles (NPs) display the white line position at a slightly higher energy region than RhCu M and RhCu M-tpp, which should be caused by surface oxidation in air. The Fourier transforms of EXAFS spectra were conducted to obtain the local coordination environments of Cu (Fig. 2*B* and *SI Appendix*, Figs. S9–S11). Different from the dominant peaks at ~2.18 Å ascribed to the Cu–Cu scattering path of Cu NPs and Cu foil in R space, both RhCu M-tpp and RhCu M show their dominant peaks at ~2.11 Å, corresponding to the Cu–Cu and/or Cu-Rh scattering paths of the first shell. This change in the metal-metal bond length indicates the formation of RhCu alloy. After tpp modification, there is a slight variation on Cu–Cu and Cu–Rh bond lengths, but it does not affect the coordination number (CN) of Cu atoms obviously in RhCu M (9) and RhCu M-tpp (8.5) (Fig. 2*C* and *SI Appendix*, Table S1). From Fig. 2*D*, RhCu M-tpp and RhCu M demonstrate similar patterns of wavelet transform (WT) of Cu K-edge EXAFS spectra, which are different from that of Cu NPs, Cu foil and CuO. Compared with RhCu M, the center of maximum intensity for RhCu M-tpp shows a slight decrease in both k and R ranges. Meanwhile, the distribution of maximum intensity for RhCu M-tpp is narrower in k range than RhCu M. These results indicate tpp modification results in a certain variation on the coordination structure of RhCu M (Fig. 2*D* and *SI Appendix*, Fig. S12). Moreover, X-ray photoelectron spectroscopy (XPS) was performed to further clarify the chemical states of heterophase RhCu M-tpp (*SI Appendix*, Fig. S13*A*). It can be seen that Rh metallic state dominates in all synthesized metallenes but both RhCu M-tpp and RhCu M have much lower proportion of Rh^{3+} than Rh M (*SI Appendix*, Fig. S13*B*). More obvious valence state changes can be found in the high-resolution XPS spectra of Cu 2p. Two strong peaks located at 931.5 and 951.5 eV are attributed to the $2p_{1/2}$ and $2p_{3/2}$ doublet of metallic Cu^0, while the other two weaker groups of double peaks at 932.5/952.4 eV and 934.2/954.1 eV represent the high-valence Cu^+ and Cu^{2+} in RhCu M-tpp (Fig. 2*E*),

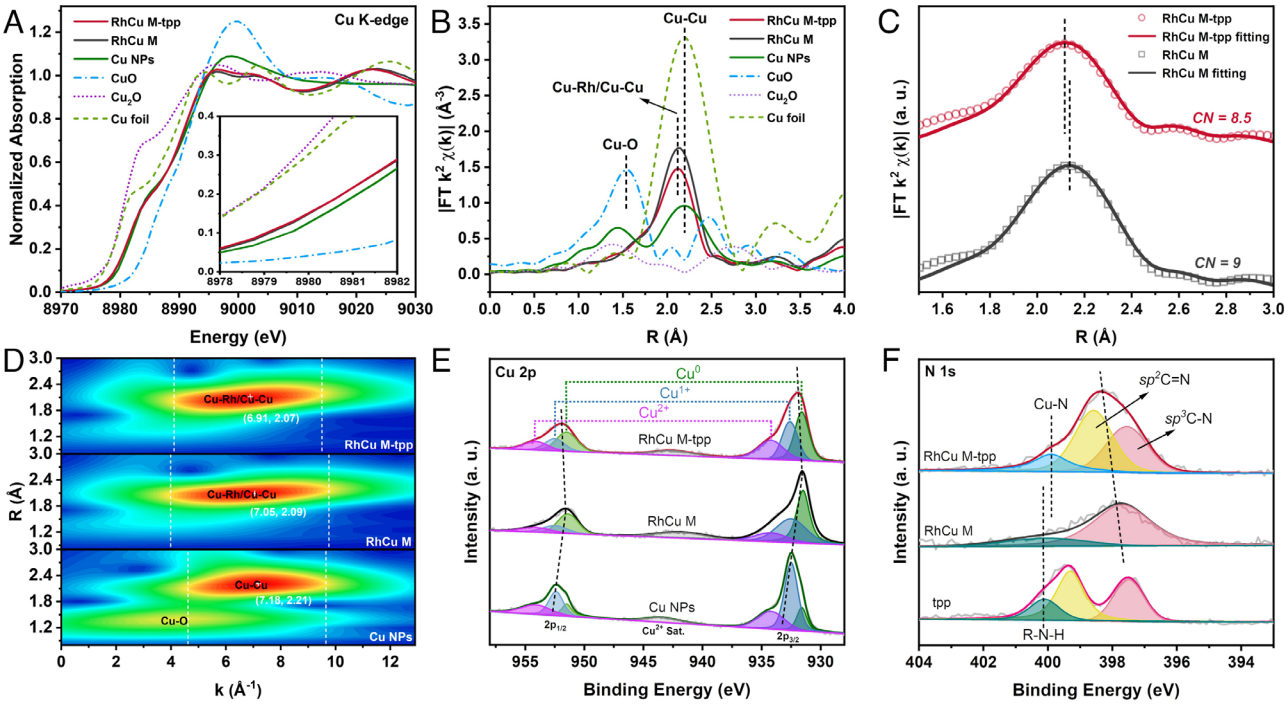

Fig. 2. X-ray spectral analysis. (*A*) Normalized Cu K-edge XANES spectra of RhCu M-tpp, RhCu M, and Cu NPs. *Inset*: The zoom-in graph showing the detailed white line positions. The data for reference samples of Cu foil, Cu_2O, and CuO are included for comparison. (*B–D*) R-space EXAFS (*B*), R-space EXAFS fitting (*C*), and wavelet transform (*D*) of RhCu M-tpp, RhCu M, and Cu NPs. (*E* and *F*) High-resolution XPS spectra of Cu 2p (*E*) and N 1 s (*F*) for RhCu M-tpp, RhCu M, and Cu NPs or tpp.

respectively (29, 32, 46). Compared with the pristine RhCu M, tpp modification induces a slight increase of Cu valence, which should be ascribed to the electron transfer from Cu in RhCu to N in tpp. The Cu LMM Auger electron spectroscopy (AES) characterization further confirms this valence state change (*SI Appendix*, Fig. S14). Such strong electron coupling is identified as the Cu-N bonds given that a characteristic peak is detected at 399.9 eV in the N 1 s XPS spectrum (Fig. 2*F*) (36, 47). Simultaneously, the appearance of sp^2-hybridized C atoms (C = N bonds) at around 398.6 eV further corroborates the existence of tpp in the obtained RhCu M-tpp (48–50).

NO_3RR and EOR Performance. To evaluate the NO_3RR performance of as-synthesized metallenes, linear sweep voltammetry (LSV) measurements were first conducted in 0.5 M Na_2SO_4 aqueous solution in the absence/presence of 3,000 ppm $NaNO_3$. Such a low-concentration (~48 mM) NO_3^--based neutral electrolyte is relatively close to the NO_3^- concentration in industrial wastewater and also greatly alleviates the CO_2 intake problem. As depicted in Fig. 3*A*, heterophase RhCu M-tpp and RhCu M deliver much higher current densities after adding NO_3^- in the electrolyte. The peak current occurring at −0.2 to −0.4 V (vs. RHE) is attributed to the limited mass transfer (30, 43, 51), in which NO_3RR and hydrogen evolution reaction (HER) compete at this stage but NO_3RR should dominate. When the applied potential becomes more negative [<−0.4 V (vs. RHE)], the competing HER process dominates due to the strong hydrogen evolution capacity of Rh. In contrast, there is a relatively small discrepancy between the LSV curves of Rh M with and without NO_3^-. Additionally, the synthesized Cu NPs deliver quite tiny current over this potential window, consistent with the reported Cu catalysts (30, 32, 38, 52).

The products of NO_3RR were analyzed by colorimetric methods (*SI Appendix*, Figs. S15 and S16). Fig. 3*B* shows the FEs of NH_3 and NO_2^- for as-synthesized samples. Apparently, RhCu M-tpp delivers the best performance over the whole potential window from −0.1 to −0.5 V (vs. RHE) and achieves excellent ammonia FE of above 70% with potential above −0.4 V and the highest ammonia FE of 84.8% at −0.2 V (vs. RHE). Meanwhile, a small proportion of NO_2^- was also detected as the byproduct of NH_3 electrosynthesis, with the FEs ranging from 3.4% to 10.9%. In comparison, RhCu M and Rh M show the distinctly inferior catalytic selectivity toward NH_3 (FE < 60.3% for RhCu M; FE < 32.6% for Rh M) as the potential decreases, especially below −0.2 V (vs. RHE). For pure Cu NPs, NO_2^- generation dominates in the nitrate reduction process, but the total FEs of NH_3 and NO_2^- still lay in a quite low level under the same test conditions. Fig. 3*C* demonstrates that the NH_3 yield rate of RhCu M-tpp continuously increases with the decrease of potential and reaches the maximum point of 717.8 mg h^{-1} g^{-1}_{cat}, which is almost 6 times that of RhCu M. This observation implies the important role of tpp in boosting the NO_3^- reduction to NH_3 on RhCu metallenes. Simultaneously, the NH_3 yield rates of Rh M and Cu NPs were even much smaller (approximately 10–30 mg h^{-1} g^{-1}_{cat}) because of the much lower ammonia FEs and current densities (*SI Appendix*, Fig. S17). The NO_2^- yield rates of above catalysts were also given here for reference (*SI Appendix*, Fig. S18). Besides, a catalytic performance comparison between this catalyst and previously reported ones for NO_3RR in neutral media has been made to highlight the superior advantages of RhCu M-tpp in the selective NH_3 electrosynthesis at low overpotentials (*SI Appendix*, Table S2) (2, 32, 36, 53, 54).

The electrochemical double-layer capacitance (C_{dl}) measurements were conducted to study the effect of tpp modification on the electrochemically active surface areas (ECSAs) of these metallenes. Under the same mass loading, RhCu M-tpp possesses a C_{dl} of 2.79 mF cm^{-2}, which is nearly twice that of RhCu M (1.47 mF cm^{-2}), suggesting that more in-plane alloy sites become active for NO_3RR after being coupled with N atoms of tpp (Fig. 3*D* and *SI Appendix*, Fig. S19). This result accounts for the much higher NH_3 yielding rate of RhCu M-tpp than RhCu M to some extent. Note that tpp itself shows neglectable catalytic

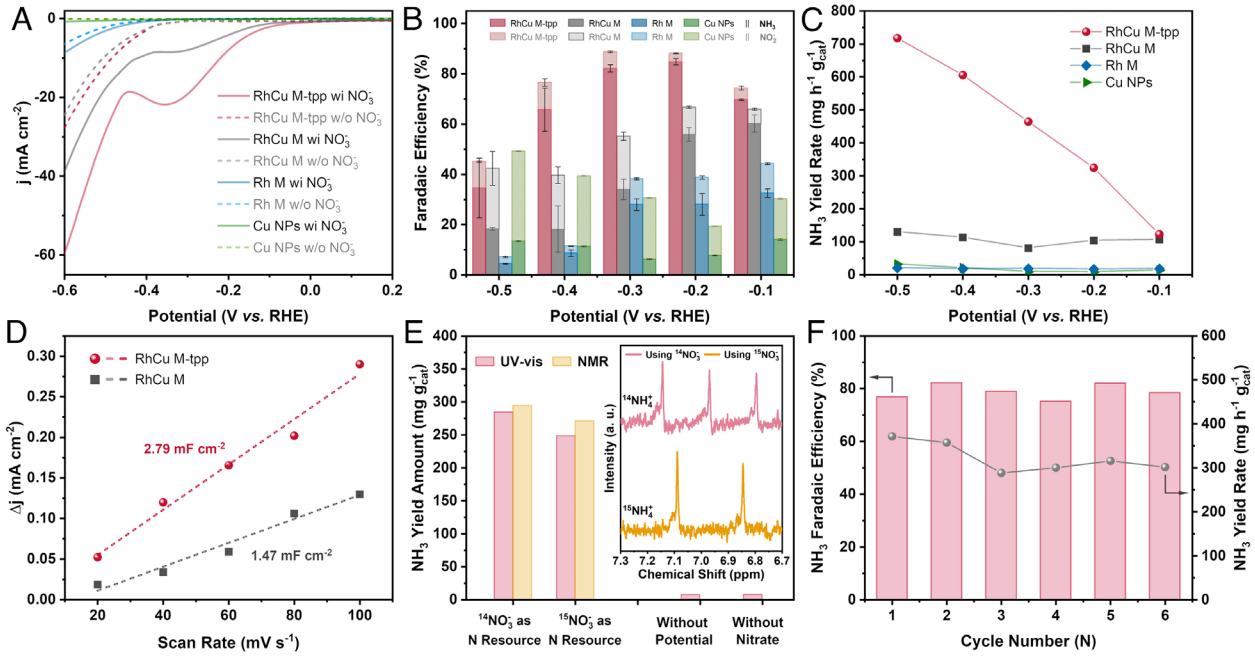

Fig. 3. Electrocatalytic NO_3RR performance. (*A*) LSV curves of RhCu M-tpp, RhCu M, Rh M, and Cu NPs in neutral 0.5 M Na_2SO_4 solution in the presence (solid lines) and absence (dashed lines) of 3,000 ppm NO_3^- at 5 mV s^{-1}. (*B* and *C*) FEs of NH_3 and NO_2^- (*B*) and NH_3 yield rates (*C*) on RhCu M-tpp, RhCu M, Rh M, and Cu NPs under different applied potentials. (*D*) Fitting results of double layer capacitance (C_{dl}) for RhCu M-tpp and RhCu M. (*E*) The NH_3 yielding amount of RhCu M-tpp after 1 h electrolysis using $^{14}NO_3^-$ or $^{15}NO_3^-$ as the nitrogen resources at −0.2 V (vs. RHE), quantified by both UV–Vis and NMR methods. The NH_3 amounts recorded in the cases without applied potential but in the presence of NO_3^- and without NO_3^- at −0.2 V (vs. RHE) are also provided. *Inset*: The ^1H NMR spectra of electrolytes after NO_3RR using $^{14}NO_3^-$ or $^{15}NO_3^-$. (*F*) FEs and yield rates of NH_3 on RhCu M-tpp during six cycles of 1 h electrolysis at −0.2 V (vs. RHE).

activity toward the NH_3 electrosynthesis (*SI Appendix*, Fig. S20). To confirm the origin of nitrogen in the synthesized NH_3, isotope labeling experiments were also performed (Fig. 3*E* and *SI Appendix*, Fig. S21). Importantly, the NH_3 yield amount in electrolytes after NO_3RR using $^{14}NO_3^-$ or $^{15}NO_3^-$ as the nitrogen resources is close to each other, as verified by both ^1H NMR or ultraviolet-visible (UV–Vis) absorption spectroscopies. In addition, the yield amount of NH_3 is neglectable in the cases without adding nitrate or applying potential. These results corroborate that the obtained NH_3 does originate from the electroreduction of NO_3^-. Furthermore, RhCu M-tpp also possesses good catalytic durability toward NH_3 synthesis (Fig. 3*F*). After the cycling stability test, the morphology, structure, and composition of RhCu M-tpp can be well maintained (*SI Appendix*, Figs. S22–S24).

Considering the formation of NH_3 results in a weak alkaline environment of the electrolyte, the EOR performance of RhCu M-tpp cathodes was further evaluated in 1 M KOH + 1 M EtOH. Carbon paper-supported RhCu M-tpp cathodes for NO_3RR were directly used for EOR measurements to approach the practical working conditions. Different from cyclic voltammetry (CV) profiles in KOH solution, both RhCu M-tpp and RhCu M exhibit two obvious ethanol oxidation peaks at 0.8 and 0.4 V (vs. RHE) in KOH solution containing EtOH (*SI Appendix*, Fig. S25 *A* and *B*). The EOR peak currents are 34.0 and 31.8 mA mg^{-1} for RhCu M and RhCu M-tpp. When conducting the chronoamperometric electrolysis at 1.0 V (vs. RHE), RhCu M-tpp demonstrates a much higher activity than RhCu M after long-term run (*SI Appendix*, Fig. S25*C*). The mass activities for RhCu M-tpp and RhCu M at different states are compared as well (*SI Appendix*, Fig. S25*D*). Importantly, after EOR measurements, most RhCu M-tpp maintains the holey and ultrathin nanostructures, in which the crystalline and amorphous domains still co-exist (*SI Appendix*, Fig. S26).

Demonstration of Rechargeable Zn-nitrate/ethanol Batteries. In light of the excellent NO_3RR performance of heterophase RhCu M-tpp at low overpotentials, the assembled routine Zn-NO_3^- batteries display a high open-circuit voltage (OCV) of ~1.4 V (vs. Zn^{2+}/Zn), which keeps stable in the next 24 h of rest period (*SI Appendix*, Fig. S27*A*). Meanwhile, the rate capability of as-fabricated batteries is excellent, which can still run normally even when the current density reaches up to 2 mA cm^{-2} (equal to ~5 A g^{-1}_{cat}) (*SI Appendix*, Fig. S27*B*). More importantly, different from the traditional Zn-NO_3^- batteries that cannot be recharged or require a high charge potential to drive OER for recharging, the rechargeability issue has been taken into consideration at the beginning of catalyst design in this work. In specific, the Rh atoms in RhCu M-tpp not only facilitate the proton enrichment around Cu sites in NO_3RR (discharge process) but also serve as active sites toward EOR (charge process) to provide electrons for reversible Zn planting on the anode. Compared with OER, EOR is more energy-economical for metal-NO_3^- batteries, in terms of the overpotential, products, and lifespan (55–57).

Based on this assumption, the mixed solution containing 0.5 M Na_2SO_4, 3,000 ppm $NaNO_3$, and 1 M ethanol was applied as the electrolyte at the cathodic side. Importantly, the introduction of ethanol does not affect the electrochemical behaviors of catalysts in NO_3RR, according to the OCV and rate performance of as-assembled Zn-nitrate/ethanol batteries (*SI Appendix*, Fig. S28 *A* and *B*). Fig. 4*A* shows the rate performance of heterophase RhCu M-tpp and Cu NP cathodes during discharging. The discharge plateaus are about 1.36, 1.28, 1.07, 0.69, 0.52, 0.41, and 0.34 V (vs. Zn^{2+}/Zn) at 0.1, 0.2, 0.5, 0.8, 1.0, 1.5, and 2.0 mA cm^{-2} for RhCu M-tpp, respectively, which are significantly higher than those of Cu NPs. Note that the apparent performance of Cu NPs mainly originates from those reactions producing NO_2^- and self-reduction rather than the one forming NH_3. When the battery went back to operation at low rates, its working voltage recovered to the pristine state, suggesting the good tolerance of RhCu M-tpp

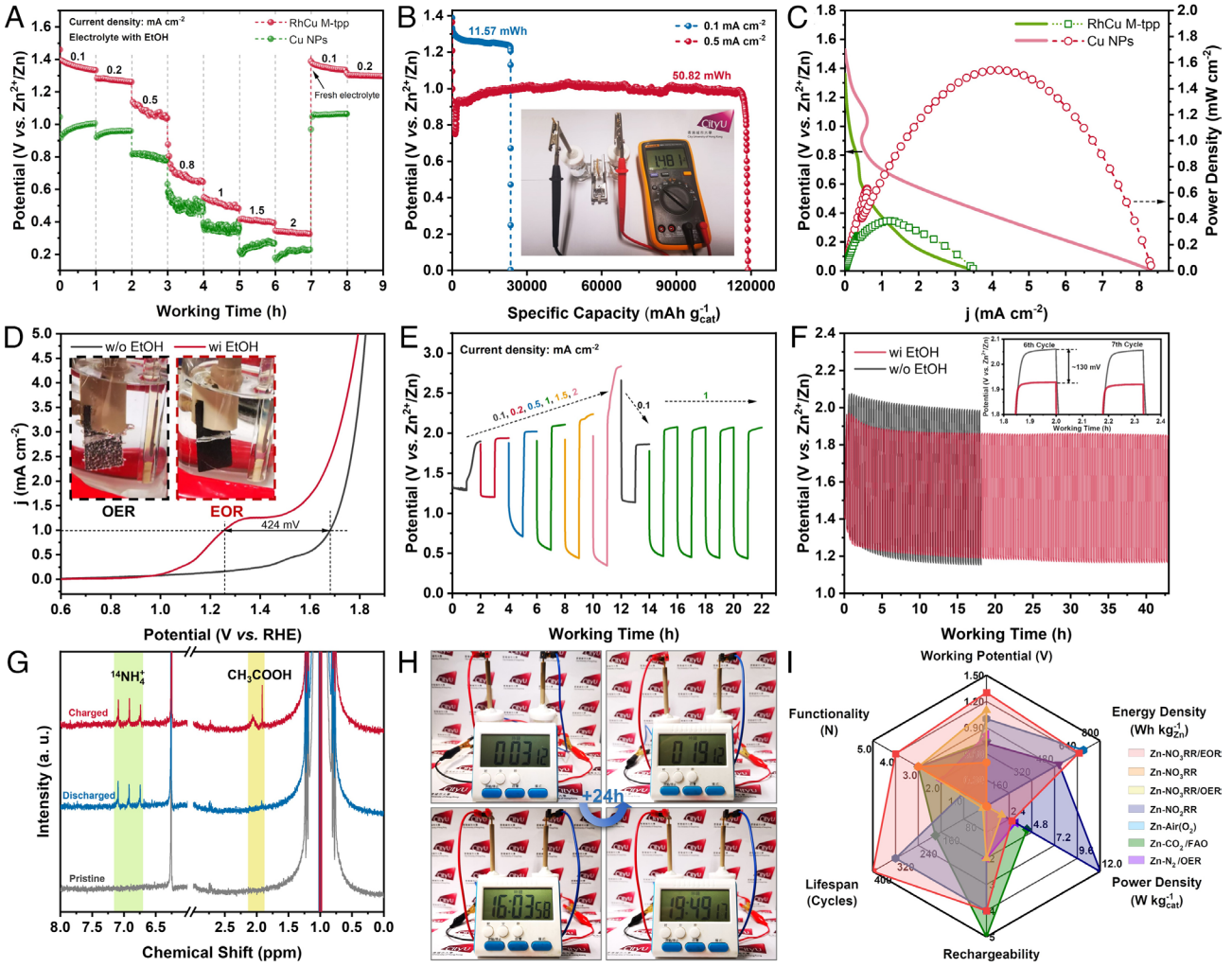

Fig. 4. Electrochemical performances of Zn-nitrate/ethanol batteries. (*A*) Rate capability of Zn-nitrate/ethanol batteries with RhCu M-tpp and Cu NPs when discharging. (*B*) Galvanostatic discharge profiles of Zn-nitrate/ethanol batteries with RhCu M-tpp cathodes from OCV to 0.005 V (vs. Zn^{2+}/Zn) at 0.1 and 0.5 mA cm^{-2}, respectively. *Inset*: A digital photograph showing the constructed battery device, along with the measurement of OCV. (*C*) Discharging polarization profiles and resultant power density curves of Zn-nitrate/ethanol batteries using RhCu M-tpp and Cu NPs. (*D*) LSV curves from 0.6 to 1.8 V (vs. RHE) of RhCu M-tpp cathodes in the electrolytes with (red line) and without (black line) ethanol after NO_3RR. *Inset*: The digital photographs of the reaction phenomena on electrodes during anodic scanning with (*Right*) and without (*Left*) ethanol, respectively. (*E*) Round-trip discharge-charge profiles of Zn-nitrate/ethanol battery with RhCu M-tpp at different current densities. (*F*) Long-term cycling stability test of as-assembled Zn-nitrate/ethanol and Zn-nitrate batteries. (*G*) The ^{1}H NMR spectra of the utilized electrolytes at the pristine, discharged and charged states. (*H*) Digital photographs of a commercial digital clock powered by the constructed Zn-nitrate/ethanol battery for continuous running above 24 h. (*I*) The comprehensive performance comparison between the as-assembled Zn-nitrate/ethanol (Zn-NO_3RR/EOR) battery and the other representative Zn-based hybridized energy storage systems.

toward high current impact. Impressively, the constructed Zn-nitrate/ethanol batteries using RhCu M-tpp can release an outstanding electric energy of 50.82 mWh in total upon fully discharged to 0.005 V (vs. Zn^{2+}/Zn) at 0.5 mA cm^{-2} (Fig. 4*B*), corresponding to a superior energy density of 117364.6 Wh kg^{-1}_{cat}. Further improvement should be feasible through increasing NO_3^- concentration and optimizing the catalyst mass loading. The discharge profile at a low rate of 0.1 mA cm^{-2} is also offered here for more comprehensive exhibition. Given the enhanced NO_3RR kinetics, Zn-nitrate/ethanol batteries with RhCu M-tpp can deliver a maximum power density of 1.54 mW cm^{-2}, which is over four times that (0.38 mW cm^{-2}) of Cu NPs (Fig. 4*C*) and also comparable to those of previously reported Zn-NO_3^- batteries using free-standing cathodes with heavy mass loadings of catalysts (20, 34, 40, 58, 59).

The introduction of ethanol into the electrolyte of Zn-NO_3^- batteries resulted in the observation of more interesting phenomena during the charge process. To verify the degradation of ethanol, we conducted the cathodic LSV measurements from OCV to 1.85 V (vs. RHE) on RhCu M-tpp cathodes after 1 h NH_3 electrosynthesis in different electrolytes with or without ethanol. Many bubbles were forming on the cathode surface during the linear scanning in the absence of ethanol, while there was no noticeable bubble formation on another cathode surface in the solution containing ethanol (Fig. 4*D*), indicating the occurring of OER and EOR in the two different electrolytes, respectively. Simultaneously, the EOR exhibited much lower overpotential than the OER at the same current density on RhCu M-tpp cathodes. At a typical current density of 1 mA cm^{-2} for battery operation, the voltage gap was as large as 424 mV, approaching the maximum value of 443 mV (*SI Appendix*, Fig. S29). It means that the energy consumption will be greatly decreased when charging this battery with EOR rather than OER. The RhCu M-tpp-based Zn-nitrate/ethanol batteries were then consecutively discharged and recharged at various rates (Fig. 4*E* and *SI Appendix*, Fig. S30*A*). As the current density increased from 0.1 to 2 mA cm^{-2}, the

gradual voltage polarizations happened in both discharge and charge processes, and the battery voltage recovered after the current density returned to 0.1 mA cm^{-2} and kept stable in the following cycles at 1 mA cm^{-2}, suggesting the good chemical and structural stability of RhCu M-tpp as a bifunctional catalyst. During the rate-capability measurements, the highest round-trip energy efficiency was 76.9% (*SI Appendix*, Fig. S30*B*). In addition, the long-term cycling performance was also evaluated in different electrolytes. Compared to the routine Zn-NO_3^- galvanic cells, the rechargeable Zn-nitrate/ethanol batteries showed a large charge plateau decrease by ~130 mV at 0.1 mA cm^{-2} and kept normal function for above 40 h (Fig. 4*F*). Furthermore, it lasted steadily for ~400 cycles when running at a higher rate of 0.5 mA cm^{-2} (*SI Appendix*, Fig. S31). The acetic acid (HAc) concentration change in the cathodic electrolyte during cycling has been further investigated by ^{1}H NMR quantification method, as shown in *SI Appendix*, Fig. S32. In particular, the HAc concentration is 408.15 mg L^{-1}, and the corresponding energy efficiency of the battery is 47.17% at the 300th cycle. As a combination of NO_3RR and EOR products, ammonium acetate, a widely used chemical in various important areas, can be generated in the cathodic electrolyte after the long-term run of Zn-nitrate/ethanol battery (Fig. 4*G*). The TEM, EDS, and XPS characterizations reveal that RhCu M-tpp is able to preserve its microstructure and surface chemical state in the long-term round-trip NO_3RR-EOR cycles after passivation (*SI Appendix*, Figs. S33–S35).

As a demonstration of its application potential in consumer electronics, the assembled Zn-nitrate/ethanol battery was utilized to power a commercial digital clock for over 24 h (Fig. 4*H*). Significantly, it is worthy to mention that few Zn-based aqueous batteries reported previously can exhibit such comprehensive performance and multifunctionality than the as-fabricated Zn-nitrate/ethanol battery (Fig. 4*I* and *SI Appendix*, Table S3) (20, 21, 34, 40, 60, 61). In general, besides some parasitic reactions like HER and OER, the plausible working principles of as-fabricated Zn-nitrate/ethanol batteries can be described as follows:

$$\text{Anode: } 4Zn + 8OH^- \rightleftharpoons 4ZnO + 4H_2O + 8e^-$$

$$\text{Cathode: } NO_3^- + 7H_2O + 8e^- \rightarrow NH_3 \cdot H_2O + 9OH^- \text{ (Discharge)}$$

$$C_2H_5OH + 4OH^- \rightarrow CH_3COOH + 3H_2O + 4e^- \text{ (Charge)}$$

$$\text{Overall reactions: } 4Zn + NO_3^- + 3H_2O \rightarrow 4ZnO + NH_3 \cdot H_2O + OH^- \text{ (Discharge)}$$

$$4ZnO + 2C_2H_5OH \rightarrow 4Zn + 2CH_3COOH + 2H_2O \text{ (Charge)}$$

$$NO_3^- + 2C_2H_5OH \rightarrow CH_3COONH_4 + CH_3COO^- + H_2O \text{ (Cycle)}$$

In addition, when EtOH is replaced by methanol (MeOH) or ethylene glycol (EG), there are similar effects on decreasing the charge plateaus of assembled Zn-nitrate/MeOH and Zn-nitrate/EG batteries (*SI Appendix*, Fig. S36). Hence, this strategy should be universal for constructing various rechargeable Zn-nitrate/alcohol batteries, where electrolytes can be customized according to the category of organic ammoniates required.

Mechanism Study of Molecule-metal Relay Catalysis. To gain deeper insights into the enhanced catalytic performance of heterophase RhCu M-tpp toward NH_3 electrosynthesis, systematic ex/in situ analysis and characterizations were carried out. Fig. 5*A* shows that NO_2^- dominates the reduction products on pure tpp electrode, while the formation of NH_3 is greatly promoted on RhCu M electrode over the entire potential window of −0.1 to −0.5 V (vs. RHE). Significantly, the combination of tpp and RhCu alloying sites gives rise to much higher selectivity toward NH_3 generation on the RhCu M-tpp cathode than that on the RhCu M counterpart. Furthermore, despite the NO_3RR rates are normalized to ECSAs (Fig. 5*B*), RhCu M-tpp still delivers much faster consumption of electrons to convert NO_3^- than RhCu M over a broad range of potentials, indicating the significantly enhanced reaction kinetics on individual active site. The above results suggest that there is a molecule-metal relay catalysis between tpp and RhCu alloying sites, with a conversion sequence of $NO_3^- \xrightarrow{tpp} NO_2^- \xrightarrow{RhCu} NH_3$. In specific, NO_3^- is first adsorbed and subsequently reduced to NO_2^- at a moderate reaction rate on tpp, and then NO_2^- will diffuse to Cu sites for the following rapid hydrogenation assisted by the surrounding Rh atoms toward NH_3 production. Meanwhile, the presence of tpp molecules on the RuCu metallene surface could also help to suppress the formation of H_2 (the primary gaseous side-product) around Rh centers under low-overpotential conditions, according to the in situ differential electrochemical mass spectrometry (DEMS) and H_2 quantification results (*SI Appendix*, Fig. S37).

The Kelvin probe force microscopy (KPFM) characterization revealed the inhomogeneous potential distribution in the 3D assembly of as-synthesized RhCu M-tpp (Fig. 5*C*), where the metallene junctions deliver the higher potential than the in-plane nanosheets. Based on the potential line scan of a typical metallene assembly, the potential gap was estimated to be approximately 36.6 mV (Fig. 5*D*). Thus, it can be deduced that several oriented electric fields are established crossing from the junction to nanosheet edge in every individual metallene under applied potentials. As a result, such gradient distribution of electric fields should be capable of facilitating the ionic migration and the adsorption/desorption of intermediates on catalyst surface, thereby promoting the reaction kinetics of NO_3RR.

To further understand the electrochemical mechanisms of NO_3RR and EOR happening on RhCu M-tpp, in situ DEMS was utilized to clarify the reaction intermediates and products of Zn-nitrate/ethanol batteries. Note that two different signals with mass-to-charge (m/z) ratios of 2 and 17 were detected as a function of reaction time when performing four times of cathodic linear sweeping from 0 to −0.66 V (vs. RHE) at 6 mV s^{-1}, corresponding to the formation of H_2 and NH_3 under negative potentials, respectively (Fig. 5*E*). Nevertheless, different from the previous relevant reports, the signals of NH_2OH (m/z = 33) and NO_2 (m/z = 46) intermediates did not appear at the NO_3RR side, which could be attributed to the extremely rapid hydrogeneration process on this molecule-metal relay catalyst. At the EOR side, there was no

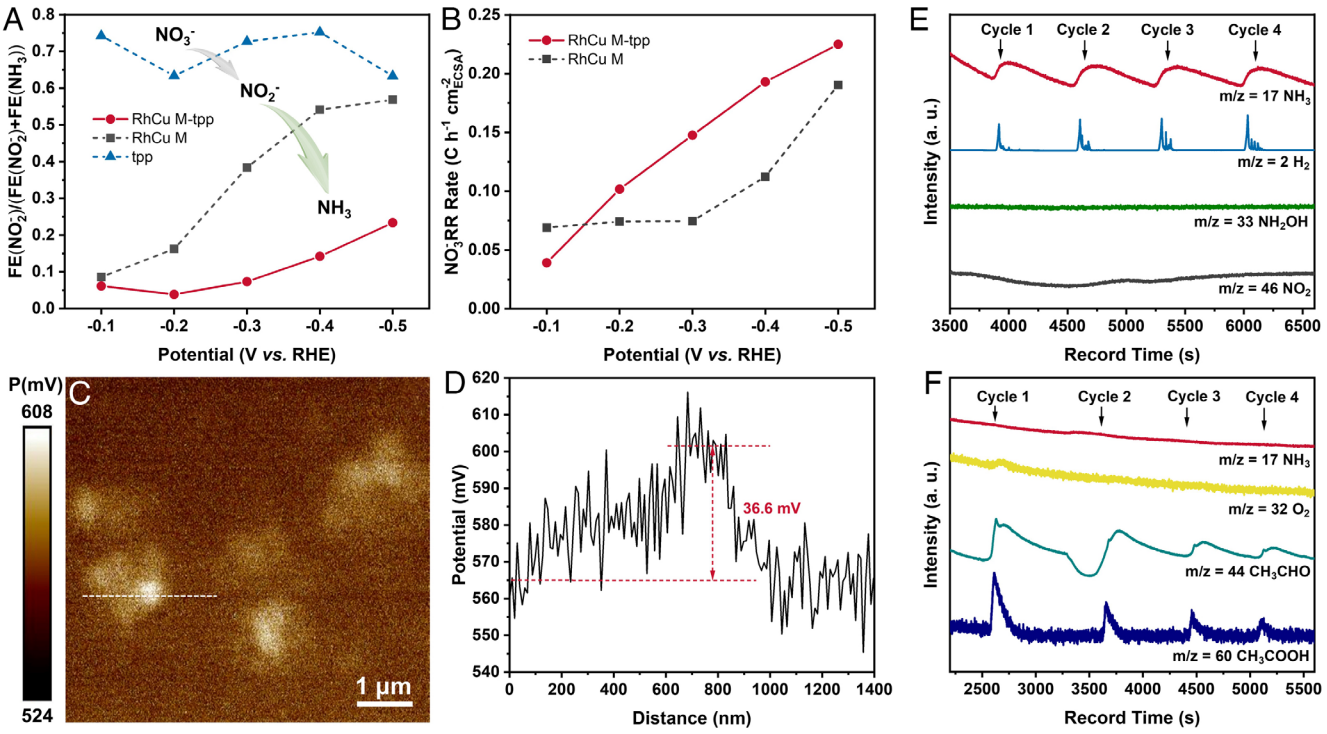

Fig. 5. Electrochemical mechanism exploration. (*A*) $\frac{FE(NO_2^-)}{FE(NO_2^-)+FE(NH_3)}$ ratios at different applied potentials for pure tpp, RhCu M, and RhCu M-tpp. (*B*) Electric quantity consumption rates of NO_3RR normalized to ECSA for RhCu M-tpp and RhCu M under different potentials. (*C* and *D*) Surface potential distribution mapping (*C*) and potential line scan (*D*) of RhCu M-tpp. (*E* and *F*) In situ DEMS patterns for RhCu M-tpp cathodes during the initial NO_3RR (*E*) and the subsequent EOR (*F*). Four periods of cathodic and anodic LSV scanning were conducted to drive the electrocatalytic reactions.

obvious fluctuation on the NH_3 signal (Fig. 5*F*), suggesting that NH_3 could not be oxidized under the four times of anodic linear sweeping from 0.551 to 1.6 V (vs. RHE). This observation reveals the feasibility of the subsequent alcohol oxidation to produce ammonium acetate. A very little amount of O_2 (m/z = 32) was recognized only at the first cycle of LSV, indicating that EOR, rather than OER, is the dominant reaction while charging the battery. Acetaldehyde (CH_3CHO, m/z = 44) and acetic acid (CH_3COOH, m/z = 60) were also detected as the dominated intermediate and final product of the EOR. In addition, based on the further in situ DEMS results under ordered cathodic and anodic linear scanning periods (*SI Appendix*, Fig. S38), the OH^- generated in the former NO_3RR is of great significance on maintaining the subsequent catalytic activity of RhCu M-tpp toward EOR during discharge-charge cycles (62). The above on-line round-trip monitoring results have well explicated the detailed electrochemical reactions occurring in the discharge and charge processes of as-assembled Zn-nitrate/ethanol batteries.

Computational Investigations. To better understand the electroactivity improvements, DFT calculations have also been conducted to investigate the electronic modulations induced by the surface tpp molecules. Considering the computational loading, we have introduced one building unit of tpp on the interface region of crystalline and amorphous RhCu. For the electronic distributions near the Fermi level (E_F), we notice that the interfacial region and surface tpp have dominated the bonding orbitals of the RhCu M-tpp surface, which play as the main active sites (Fig. 6*A*). Compared to the RhCu M, the bonding orbitals become much stronger at the interfacial region between the crystalline and amorphous parts, which supports the increase of active sites for NO_3RR (Fig. 6*B*). The coverage of tpp molecules on the surface is able to activate the electroactivity of the surface regions to offer more accessible active sites. These results show that the abundant crystal–amorphous interfaces and surface tpp modifications are significant to guarantee highly electroactive surface and efficient electron transfer efficiency from catalysts to the adsorbates. The interface remains stable after geometry optimizations, indicating the good overall stability of the catalysts. In order to reveal the electronic structures, we have demonstrated the projected partial density of states (PDOSs) (Fig. 6*C*). It is noted that Cu-3d orbitals locate near E_V – 2.18 eV (Ev = 0 eV) with good orbital coupling with Rh-4d orbitals. Meanwhile, Rh-4d orbitals cover the Cu-3d orbitals and cross the E_F with e_g-t_{2g} splitting of 2.97 eV to facilitate electron transfer. This electronic structure supplies a highly robust electroactivity of active sites during NO_3RR. The introduction of surface tpp not only further increases the electron density near E_F to accelerate the electron transfer but also offers broad *p* orbital distributions to improve the adsorption of NO_3^- through *p*–*p* couplings. Such strong adsorption of NO_3^- on surface tpp is further demonstrated by the PDOSs (Fig. 6*D*). Notably, the downshifting of *s,p* orbitals of NO_3^- is noted, supporting the electron transfer from the RhCu M-tpp to the adsorbates. For the free NO_3^-, the good overlapping of *s,p* orbitals with the tpp molecule is observed, especially near E_V – 6.0 eV to E_V – 8.0 eV, which induces the stable binding and activation of NO_3^- to accelerate the following reduction steps. Then, we further unravel the site-dependent PDOSs of both Cu and Rh sites in different parts of RhCu M-tpp (Fig. 6*E*). For the Cu sites in the crystalline RhCu part, the Cu-3d orbitals exhibit a gradual upshifting trend from the bulk to the surface, leading to the improved d-band center and electroactivity. In particular, we notice that the introduction of tpp results in the upshifted Cu-3d orbitals, which is consistent with the XPS result that the valence state of Cu sites is slightly enlarged (Fig. 2*E*). The electronic structure evolutions of Cu-3d become even stronger in the amorphous part.

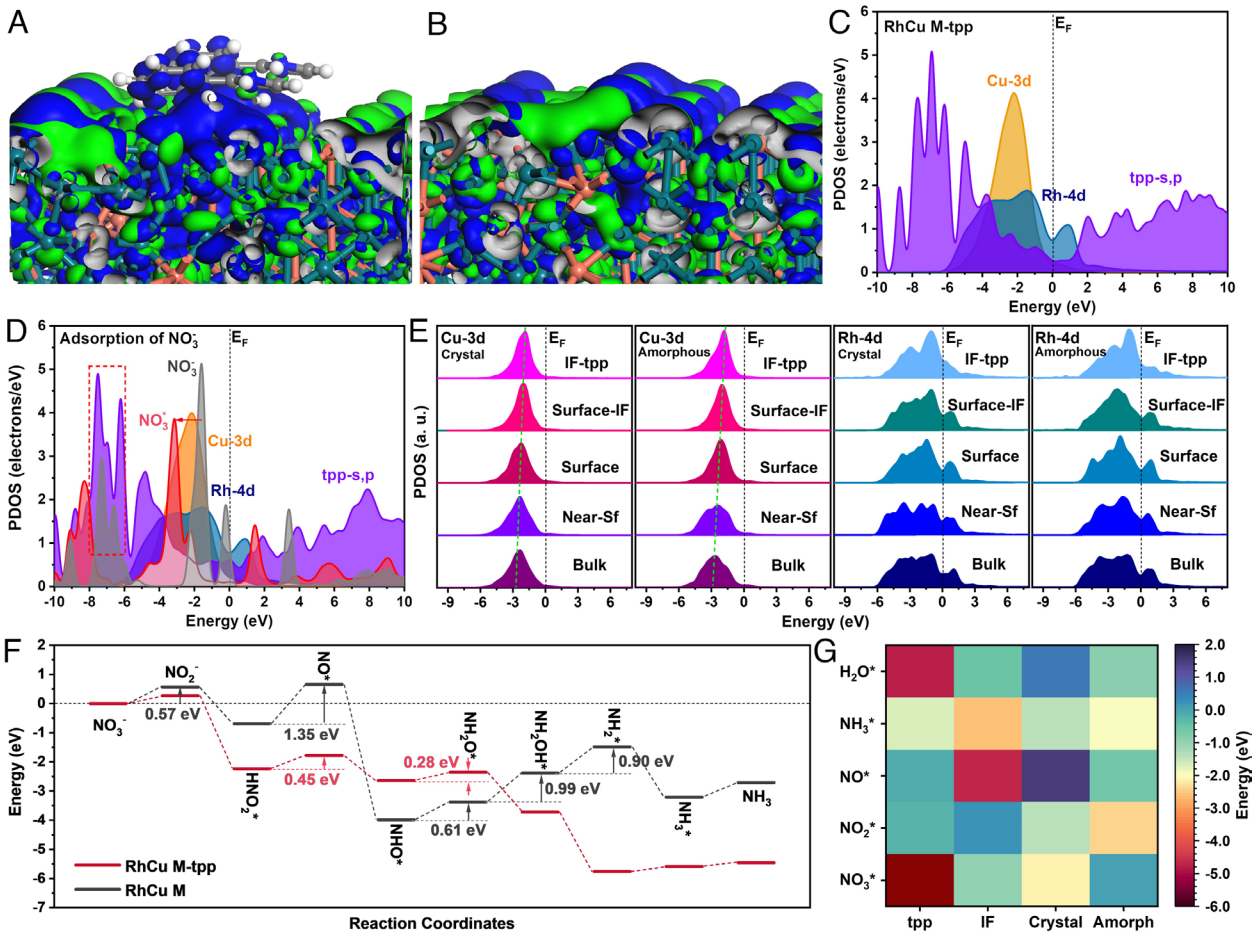

Fig. 6. Computational studies. (*A* and *B*) The 3D contour plots of electronic distributions near the Fermi level of (*A*) RhCu M-tpp and (*B*) RhCu M. Teal balls = Rh, orange balls = Cu, gray balls = C, blue balls = N, and white balls = H. Blue isosurface = bonding orbitals, and green isosurface = anti-bonding orbitals. (*C*) PDOSs of RhCu M-tpp. (*D*) PDOSs of NO_3^- adsorption on RhCu M-tpp. (*E*) The site-dependent PDOSs of Cu-3d in crystal and amorphous parts (*Left* two panels) and Rh-4d in crystal and amorphous parts (*Right* two panels) in RhCu M-tpp. (*F*) The reaction energy comparisons of nitrate reduction on RhCu M-tpp and RhCu M. (*G*) The adsorption energy comparisons of key intermediates on different sites of RhCu M-tpp. IF = interface, Crystal = crystal part of RhCu, Amorph = amorphous part of RhCu.

The bulk Cu-3d shows evidently a lower position than that of the surface Cu sites. However, compared to the crystalline part, the Cu-3d orbitals locate closer to the E_F in the amorphous part, indicating that the amorphous part plays a significant role in promoting the electroactivity of surface interfacial regions. For the Rh-4d orbitals in the crystalline structures, the e_g-t_{2g} splitting has been gradually alleviated from the bulk to the surface. After the introduction of tpp, the e_g-t_{2g} splitting is significantly reduced with enhanced electron density near E_F, leading to faster site-to-site electron transfer in RhCu M-tpp. For the amorphous part, the e_g-t_{2g} splitting of Rh-4d orbitals delivers a volcano trend, which increases first at the surface and reduces at the interface sites with tpp. This proves that the surface modification of RhCu M with tpp is critical to ensure electron transfer on the catalyst surface.

The reaction energy of NO_3RR has been compared between RhCu M-tpp and RhCu M to indicate the importance of tpp (Fig. 6*F*). Notably, the activation barriers for the conversion of nitrate to NO_2* have been reduced from 0.57 eV to 0.26 eV due to the introduction of tpp on the RhCu M. The largest energy barrier is observed at the conversion from HNO_2* to NO* for both RhCu M-tpp and RhCu M. RhCu M demonstrates a continuous uphill trend from NHO* to NH_2*, which largely lowers the electrocatalytic performance. In contrast, RhCu M-tpp only shows one minor barrier of 0.28 eV from NHO* to NH_2O, supporting a highly efficient nitrate reduction. Moreover, the desorption of generated NH_3 displays an energy barrier of only 0.13 eV on RhCu M-tpp, which is much smaller than that on RhCu M (0.50 eV), offering a fast generation of NH_3. To reveal the reaction trends of NO_3RR, the adsorption energies of different key intermediates are compared on different sites of RhCu M-tpp (Fig. 6*G* and *SI Appendix*, Table S4). For the initial reactants, it is noted that both NO_3^- and H_2O are much more preferred to adsorb on the tpp sites, which benefits the activations of nitrate and dissociation of water. In the meantime, the adsorption of NO_2* and NO* becomes more energetically favored on the amorphous and interfacial sites of the catalyst surface, respectively, indicating the following nitrate reduction process is promoted on the RhCu surface. The adsorption results support that the nitrate reduction process on RhCu M-tpp is potentially a cascade catalysis, where the surface tpp guarantees the activation of nitrate while the RhCu plays as the active site for the subsequent reduction from NO_2^- to the final product NH_3.

Discussion

In summary, we have successfully synthesized an efficient bifunctional catalyst of holey heterophase RhCu M-tpp for low-overpotential NH_3 electrosynthesis and ethanol oxidation. The obtained RhCu M-tpp demonstrated excellent NO_3RR selectivity toward NH_3 in neutral media over a broad potential window of

–0.1 to –0.4 V (vs. RHE), with the highest FE_{NH3} of up to 84.8% at –0.2 V (vs. RHE). Benefitting from the good electrocatalytic activity of RhCu M-tpp toward both NO_3RR and EOR, a rechargeable Zn-nitrate/ethanol battery was constructed, which delivered an outstanding energy density of 117364.6 Wh kg^{-1}_{cat}, ultralow discharge-charge voltage difference, superior long-term cycling stability of ~400 cycles, and potential ammonium acetate production. Experimental studies and DFT calculations have unraveled that the surface tpp is able to supply highly electroactive sites to improve the adsorption of NO_3^- through the *p–p* orbital coupling. Meanwhile, the electroactivity of abundant interface regions also promotes the following reduction from NO_2^- to NH_3. Compared to RhCu M, the interfacial modulations and tpp modification synergistically contribute to the greatly improved performances of nitrate reduction. This work not only highlights the significance of molecule-metal relay catalysis to efficient NH_3 electrosynthesis in NO_3RR but also offers a multifunctional battery prototype to reveal the merits of metal-based hybrid electrochemical systems on the high-performance and sustainable energy storage and conversion.

Materials and Methods

Synthesis of Heterophase RuCu M, Rh M, Cu NPs, and RhCu M-tpp. In a typical synthesis of RhCu M, 3,200 μL of OAm, 800 μL of $Rh(acac)_3$ solution (5 mM, in OAm), 400 μL of KI solution (40 mM, in 1, 2-BDO), and 200 μL of $Cu(acac)_2$ solution (5 mM, in OAm) were mixed together in a 20-mL glass vial and then stirred for 10 min. After that, the glass bottle was sealed and subjected to heat treatment in oil bath at 160 °C for 12 h. After reaction, the sediments were collected and washed with the mixture of n-hexane and ethanol with a volume ratio of 1/1 for several times. The Rh M was synthesized through the same procedure but without adding the $Cu(acac)_2$/OAm solution. As for the synthesis of Cu NPs, 10 mL of $Cu(acac)_2$ solution (10 mM, in OAm) and 1 mL of 1,2-BDO were added into a 12-mL glass bottle, followed by heat treatment in oil bail at 140 °C for 3 h. Then, Cu NPs could be obtained by centrifugation. RhCu M-tpp was prepared by a facile ligand exchange method. Typically, ~3 mg of RhCu M was dispersed in 10 mL of chloroform added with 10 mg of tpp. The slurry was kept stirring for 24 h at room temperature for sufficient ligand exchange. Finally, the sediments were collected by centrifugation and washed with chloroform/ethanol (v/v = 1/1) solution for several times. More preparation details are described in *SI Appendix*.

Electrocatalytic NO_3RR Measurements. The synthesized catalysts were directly mixed with Nafion (5%$_{wt}$ in isopropanol) at a catalyst/binder weight ratio of 5/1 without introducing any carbon conductors. A certain amount of isopropanol was utilized as the solvent to prepare the homogenous catalyst ink with a catalyst concentration of ~1 mg mL^{-1} through sonication. The obtained catalyst ink was dropped onto the carbon paper plates (CP, 1 × 1 cm, Toray H-060) slowly and homogenously at ambient environment. The mass loadings were controlled within 0.4 to 0.5 mg cm^{-2}. All the NO_3RR performances were evaluated in H-cells separated by activated Nafion 117 membranes in ambient environment. The CP-supported catalysts, Ag/AgCl electrode, and platinum (Pt) plate (1 × 1 cm^2) were used as the working electrode, reference electrode, and counter electrode, respectively. An Ar-saturated solution containing 0.5 M Na_2SO_4 and 3,000 ppm $NaNO_3$ acted as both the cathodic and anodic electrolytes. Chronoamperometry (CA) tests were conducted at a series of different applied potentials with 85% IR compensation under a stirring rate of 600 rpm to accelerate mass transfer.

Assembly of Rechargeable Zn-nitrate/ethanol Batteries and Zn-nitrate Galvanic Cells. When assembling rechargeable Zn-nitrate/ethanol batteries, CP-supported catalysts (1 × 1 cm) were used as the working electrodes and polished Zn plates (2 × 2 cm) worked as the both reference and counter electrodes. A bipolar membrane was employed as the separator to isolate the cathodic and anodic electrolytes in a typical H-cell. Of note, 25 mL of 1 M KOH aqueous solution with 0.02 M $Zn(CH_3COO)_2$ as additive played as the anodic electrolyte while another 25 mL of 0.5 M Na_2SO_4/3,000 ppm NO_3^- solution mixed with 1 M EtOH played as the cathodic one. The assembly of routine Zn-nitrate galvanic cells is similar to that of above rechargeable Zn-nitrate/ethanol batteries but only using 0.5 M Na_2SO_4/3,000 ppm NO_3^- mixed solution as the cathodic electrolyte.

Characterization. XRD measurements were conducted on a Rigaku SmartLab SE X-ray diffractometer. SEM and EDS data were acquired by a Thermo Fisher Scientific (TFS) Quattro S scanning electron microscope. TEM images and EELS spectra were collected on a field emission JEM-2100F (JEOL, Japan). The HAADF-STEM images and EDS elemental mappings were obtained on a double aberration-corrected Spectra 300 TEM/STEM (TFS). The order of magnitude of the electron dose is down to the 10^3 e^- $Å^{-2}$. The FT-IR spectra were recorded on a Bruker TENOR 27 spectrophotometer employing the KBr pellets. The product analysis was made using NMR spectroscopy (300 MHz, Bruker AVANCE III BBO Probe) and ultraviolet-visible absorbance spectroscopy (UV–Vis spectrophotometer, SHIMADZU UV-2600). XPS analysis was based on a ESCALAB 220i-XL electron spectrometer from VG Scientific using 300 W Al KR radiation. X-ray absorption spectroscopy (XAS) was conducted in a transmission mode at beamline X-ray absorption fine structure for catalysis (XAFCA) of Singapore Synchrotron Light Source.

Theoretical Calculations. To construct the crystalline part of RhCu M, we have cleaved the (110) surface from the Rh unit cell with 6 atomic layers, where the thickness is less than 1 nm to match the experiments. To match the atomic ratio of 3:1, 25 % of the Rh sites have been replaced with Cu atoms. For the amorphous part of RhCu M, we have carried out molecular dynamic (MD) simulations under 1,200 K for 5 ps with 1 fs for each step. The MD simulations were carried out under the NVT condition with constant temperature and volume. The RhCu M was constructed by half crystalline part and half amorphous part with 120 atoms ($Rh_{90}Cu_{30}$) in total. Considering the large size of the tpp molecule, we have only introduced the building unit of tpp on the interface within RhCu M. A vacuum space of 20 Å along the z-axis direction was also introduced to guarantee sufficient space during the relaxation process. More calculation details are provided in *SI Appendix*.

Data, Materials, and Software Availability. All study data are included in the article and/or *SI Appendix*.

ACKNOWLEDGMENTS. This work was supported by grants (Project Nos. 22175148, 22005258, and 52102320) from National Natural Science Foundation of China, grant (Project Nos. 21309322 and 15307522) from Research Grants Council of Hong Kong, grant (Project No. JCYJ20220530140815035) from Shenzhen Science and Technology Program, Innovation and Technology Commission via Hong Kong Branch of National Precious Metals Material Engineering Research Center, and grants (Project Nos. 9610480 and 9680301) from City University of Hong Kong. The Transmission Electron Microscope facility is funded by the Research Grants Council of Hong Kong (Project No. C5029-18E).

Author affiliations: [a]Department of Chemistry, City University of Hong Kong, Kowloon 999077, Hong Kong, Special Administrative Region of China; [b]Hong Kong Branch of National Precious Metals Material Engineering Research Center, City University of Hong Kong, Kowloon 999077, Hong Kong, Special Administrative Region of China; [c]Institute of Chemical Materials, China Academy of Engineering Physics, Mianyang 621900, China; [d]Department of Applied Biology and Chemical Technology, The Hong Kong Polytechnic University, Kowloon 999077, Hong Kong, Special Administrative Region of China; [e]Department of Applied Physics Research Institute for Smart Energy, The Hong Kong Polytechnic University, Kowloon 999077, Hong Kong, Special Administrative Region of China; [f]College of Materials Science and Engineering, Shenzhen University, Shenzhen 518060, China; [g]School of Material Science and Engineering, Tianjin University, Tianjin 300350, China; [h]Institute of Sustainability for Chemicals, Energy and Environment, A*STAR, Singapore 627833, Singapore; and [i]City University of Hong Kong Shenzhen Research Institute, Shenzhen 518057, China

Author contributions: J.Z. and Z.F. designed research; J.Z., Y.X., M.S., Z.X., Y.W., P.L., F.L., F.H., T.F., Y.M., J.Y., C.Y., B.C., S.X., Y.Z., B.H., and Z.F. performed research; J.Z., Y.X., M.S., Z.X., Y.W., S.X., Y.Z., B.H., and Z.F. analyzed data; and J.Z., M.S., and Z.F. wrote the paper.

The authors declare no competing interest.

This article is a PNAS Direct Submission.

1. Y. Ohki *et al.*, Nitrogen reduction by the Fe sites of synthetic [Mo_3S_4Fe] cubes. *Nature* **607**, 86–90 (2022).
2. G.-F. Chen *et al.*, Electrochemical reduction of nitrate to ammonia via direct eight-electron transfer using a copper-molecular solid catalyst. *Nat. Energy* **5**, 605–613 (2020).
3. Y. Xiong *et al.*, Electrochemical nitrate reduction: Ammonia synthesis and the beyond. *Adv. Mater*, 10.1002/adma.202304021, (2023).
4. A. J. Martín, T. Shinagawa, J. Pérez-Ramírez, Electrocatalytic reduction of nitrogen: From Haber-Bosch to ammonia artificial leaf. *Chem* **5**, 263–283 (2019).
5. H. Xu, Y. Ma, J. Chen, W. X. Zhang, J. Yang, Electrocatalytic reduction of nitrate–A step towards a sustainable nitrogen cycle. *Chem. Soc. Rev.* **51**, 2710–2758 (2022).
6. J. Gao *et al.*, Electrocatalytic upcycling of nitrate wastewater into an ammonia fertilizer via an electrified membrane. *Environ. Sci. Technol.* **56**, 11602–11613 (2022).
7. J. Zhou *et al.*, Boosting the reaction kinetics in aprotic lithium-carbon dioxide batteries with unconventional phase metal nanomaterials. *Proc. Natl. Acad. Sci. U.S.A.* **119**, e2204666119 (2022).
8. B. Lu *et al.*, Engineering the interfacial orientation of MoS_2/Co_9S_8 bidirectional catalysts with highly exposed active sites for reversible Li-CO_2 batteries. *Proc. Natl. Acad. Sci. U.S.A.* **120**, e2216933120 (2023).
9. J. Zhou, J. Cheng, B. Wang, H. Peng, J. Lu, Flexible metal-gas batteries: A potential option for next-generation power accessories for wearable electronics. *Energy Environ. Sci.* **13**, 1933–1970 (2020).
10. Y. Wang *et al.*, Decreasing the overpotential of aprotic Li-CO_2 batteries with the in-plane alloy structure in ultrathin 2D Ru-based nanosheets. *Adv. Funct. Mater.* **32**, 2202737 (2022).
11. Y. Ma *et al.*, Surface modification of metal materials for high-performance electrocatalytic carbon dioxide reduction. *Matter* **4**, 888–926 (2021).
12. Z. Fan *et al.*, Heterophase fcc-2H-fcc gold nanorods. *Nat. Commun.* **11**, 3293 (2020).
13. B. Chen *et al.*, Designing electrophilic and nucleophilic dual centers in the ReS_2 plane toward efficient bifunctional catalysts for Li-CO_2 batteries. *J. Am. Chem. Soc.* **144**, 3106–3116 (2022).
14. V. Kyriakou, I. Garagounis, E. Vasileiou, A. Vourros, M. Stoukides, Progress in the electrochemical synthesis of ammonia. *Catal. Today* **286**, 2–13 (2017).
15. V. Kyriakou, I. Garagounis, A. Vourros, E. Vasileiou, M. Stoukides, An electrochemical Haber-Bosch process. *Joule* **4**, 142–158 (2020).
16. Y. Wang, Y. Yu, R. Jia, C. Zhang, B. Zhang, Electrochemical synthesis of nitric acid from air and ammonia through waste utilization. *Natl. Sci. Rev.* **6**, 730–738 (2019).
17. C. Lv *et al.*, An amorphous noble-metal-free electrocatalyst that enables nitrogen fixation under ambient conditions. *Angew. Chem. Int. Ed.* **57**, 6073–6076 (2018).
18. Z. Geng *et al.*, Achieving a record-high yield rate of 120.9 μg_{NH3} $mg_{cat.}^{-1}$ h^{-1} for N_2 electrochemical reduction over Ru single-atom catalysts. *Adv. Mater.* **30**, 1803498 (2018).
19. B. Chen, X. Zhong, G. Zhou, N. Zhao, H. M. Cheng, Graphene-supported atomically dispersed metals as bifunctional catalysts for next-generation batteries based on conversion reactions. *Adv. Mater.* **34**, 2105812 (2022).
20. Y. Guo *et al.*, Pd doping-weakened intermediate adsorption to promote electrocatalytic nitrate reduction on TiO_2 nanoarrays for ammonia production and energy supply with zinc-nitrate batteries. *Energy Environ. Sci.* **14**, 3938–3944 (2021).
21. W. Sun *et al.*, A rechargeable zinc-air battery based on zinc peroxide chemistry. *Science* **371**, 46–51 (2021).
22. D. He *et al.*, Regulation of the electrocatalytic nitrogen cycle based on sequential proton–electron transfer. *Nat. Catal.* **5**, 798–806 (2022).
23. Y. Wang *et al.*, Atomic coordination environment engineering of bimetallic alloy nanostructures for efficient ammonia electrosynthesis from nitrate. *Proc. Natl. Acad. Sci. U.S.A.* **120**, e2306461120 (2023).
24. F. Liu, Z. Fan, Defect engineering of two-dimensional materials for advanced energy conversion and storage. *Chem. Soc. Rev.* **52**, 1723–1772 (2023).
25. Y. Wang, C. Wang, M. Li, Y. Yu, B. Zhang, Nitrate electroreduction: Mechanism insight, in situ characterization, performance evaluation, and challenges. *Chem. Soc. Rev.* **50**, 6720–6733 (2021).
26. K. Fan *et al.*, Active hydrogen boosts electrochemical nitrate reduction to ammonia. *Nat. Commun.* **13**, 7958 (2022).
27. H. Wang *et al.*, Cu/CuO_x in-plane heterostructured nanosheet arrays with rich oxygen vacancies enhance nitrate electroreduction to ammonia. *ACS Appl. Mater. Inter.* **14**, 34761–34769 (2022).
28. J. Leverett *et al.*, Tuning the coordination structure of Cu-N-C single atom catalysts for simultaneous electrochemical reduction of CO_2 and NO_3^- to urea. *Adv. Energy Mater.* **12**, 2201500 (2022).
29. H. Liu *et al.*, Efficient electrochemical nitrate reduction to ammonia with copper-supported rhodium cluster and single-atom catalysts. *Angew. Chem. Int. Ed.* **61**, e202202556 (2022).
30. Y. Wang *et al.*, Enhanced nitrate-to-ammonia activity on copper-nickel alloys via tuning of intermediate adsorption. *J. Am. Chem. Soc.* **142**, 5702–5708 (2020).
31. W. He *et al.*, Splicing the active phases of copper/cobalt-based catalysts achieves high-rate tandem electroreduction of nitrate to ammonia. *Nat. Commun.* **13**, 1129 (2022).
32. Y. Wang, W. Zhou, R. Jia, Y. Yu, B. Zhang, Unveiling the activity origin of a copper-based electrocatalyst for selective nitrate reduction to ammonia. *Angew. Chem. Int. Ed.* **59**, 5350–5354 (2020).
33. H. Du *et al.*, Durable electrocatalytic reduction of nitrate to ammonia over defective pseudobrookite Fe_2TiO_5 nanofibers with abundant oxygen vacancies. *Angew. Chem. Int. Ed.* **62**, e202215782 (2023).
34. R. Zhang *et al.*, A Zn–nitrite battery as an energy-output electrocatalytic system for high-efficiency ammonia synthesis using carbon-doped cobalt oxide nanotubes. *Energy Environ. Sci.* **15**, 3024–3032 (2022).
35. X. Zhu *et al.*, Filling mesopores of conductive metal–organic frameworks with Cu clusters for selective nitrate reduction to ammonia. *ACS Appl. Mater. Inter.* **14**, 32176–32182 (2022).
36. X. F. Cheng *et al.*, Coordination symmetry breaking of single-atom catalysts for robust and efficient nitrate electroreduction to ammonia. *Adv. Mater.* **34**, 2205767 (2022).
37. Z. Fan, H. Zhang, Crystal phase-controlled synthesis, properties and applications of noble metal nanomaterials. *Chem. Soc. Rev.* **45**, 63–82 (2016).
38. J. Yang *et al.*, Potential-driven restructuring of Cu single atoms to nanoparticles for boosting the electrochemical reduction of nitrate to ammonia. *J. Am. Chem. Soc.* **144**, 12062–12071 (2022).
39. W. Wen, P. Yan, W. Sun, Y. Zhou, X. Y. Yu, Metastable phase Cu with optimized local electronic state for efficient electrocatalytic production of ammonia from nitrate. *Adv. Funct. Mater.* **33**, 2212236 (2022).
40. R. Zhang *et al.*, Efficient ammonia electrosynthesis and energy conversion through a Zn-nitrate battery by iron doping engineered nickel phosphide catalyst. *Adv. Energy Mater.* **12**, 2103872 (2022).
41. F. Lv *et al.*, Near-unity electrochemical conversion of nitrate to ammonia on crystalline nickel porphyrin-based covalent organic frameworks. *Energy Environ. Sci.* **16**, 201–209 (2023).
42. B. Qiao *et al.*, Highly active hollow RhCu nanoboxes toward ethylene glycol electrooxidation. *Small* **17**, 2006534 (2021).
43. Z. X. Ge *et al.*, Interfacial engineering enhances the electroactivity of frame-like concave RhCu bimetallic nanocubes for nitrate reduction. *Adv. Energy Mater.* **12**, 2103916 (2022).
44. F. Y. Chen *et al.*, Efficient conversion of low-concentration nitrate sources into ammonia on a Ru-dispersed Cu nanowire electrocatalyst. *Nat. Nanotechnol.* **17**, 759–767 (2022).
45. S. C. Lin *et al.*, Operando time-resolved X-ray absorption spectroscopy reveals the chemical nature enabling highly selective CO_2 reduction. *Nat. Commun.* **11**, 3525 (2020).
46. Y. Ma *et al.*, Confined growth of silver-copper Janus nanostructures with 100 facets for highly selective tandem electrocatalytic carbon dioxide reduction. *Adv. Mater.* **34**, 2110607 (2022).
47. Y. Liang *et al.*, Stabilizing copper sites in coordination polymers toward efficient electrochemical C-C coupling. *Nat. Commun.* **14**, 474 (2023).
48. J. M. Stillahn, K. J. Trevino, E. R. Fisher, Deposition of amorphous CN_X materials in BrCN plasmas: Exploring adhesion behavior as an indicator of film properties. *ACS Appl. Mater. Inter.* **3**, 1402–1410 (2011).
49. H. Li, S. Gan, H. Wang, D. Han, L. Niu, Intercorrelated superhybrid of AgBr supported on graphitic-C_3N_4-decorated nitrogen-doped graphene: High engineering photocatalytic activities for water purification and CO_2 reduction. *Adv. Mater.* **27**, 6906–6913 (2015).
50. W. Wang *et al.*, Formation of B-N-C coordination to stabilize the exposed active nitrogen atoms in g-C_3N_4 for dramatically enhanced photocatalytic ammonia synthesis performance. *Small* **16**, 1906880 (2020).
51. O. Q. Carvalho *et al.*, Role of electronic structure on nitrate reduction to ammonium: A periodic journey. *J. Am. Chem. Soc.* **144**, 14809–14818 (2022).
52. J. Sun, H. Yang, W. Gao, T. Cao, G. Zhao, Diatomic Pd-Cu metal–phosphorus sites for complete N≡N bond formation in photoelectrochemical nitrate reduction. *Angew. Chem. Int. Ed.* **61**, e202211373 (2022).
53. Z. Y. Wu *et al.*, Electrochemical ammonia synthesis via nitrate reduction on Fe single atom catalyst. *Nat. Commun.* **12**, 2870 (2021).
54. J. Li *et al.*, Atomically dispersed Fe atoms anchored on S and N-codoped carbon for efficient electrochemical denitrification. *Proc. Natl. Acad. Sci. U.S.A.* **118**, e2105628118 (2021).
55. Z. Li *et al.*, In situ electrochemical activation of $Co(OH)_2$@$Ni(OH)_2$ heterostructures for efficient ethanol electrooxidation reforming and innovative zinc-ethanol-air batteries. *Energy Environ. Sci.* **15**, 5300–5312 (2022).
56. Q. Mao *et al.*, In situ reconstruction of partially hydroxylated porous Rh metallene for ethylene glycol-assisted seawater splitting. *Adv. Funct. Mater.* **32**, 2201081 (2022).
57. X. Zhou *et al.*, Preparation of Au@Pd core-shell nanorods with fcc-2H-fcc heterophase for highly efficient electrocatalytic alcohol oxidation. *J. Am. Chem. Soc.* **144**, 547–555 (2022).
58. H. Jiang *et al.*, Enabled efficient ammonia synthesis and energy supply in a zinc-nitrate battery system by separating nitrate reduction process into two stages. *Angew. Chem. Int. Ed.* **62**, e202218717 (2023).
59. J. Liang *et al.*, Amorphous boron carbide on titanium dioxide nanobelt arrays for high-efficiency electrocatalytic NO reduction to NH_3. *Angew. Chem. Int. Ed.* **61**, e202202087 (2022).
60. L. Han *et al.*, Chemically coupling SnO_2 quantum dots and MXene for efficient CO_2 electroreduction to formate and Zn-CO_2 battery. *Proc. Natl. Acad. Sci. U.S.A.* **119**, e2207326119 (2022).
61. H. Wang *et al.*, Exfoliated metallic niobium disulfate nanosheets for enhanced electrochemical ammonia synthesis and Zn-N_2 battery. *Appl. Catal. B* **270**, 118892 (2020).
62. Y. Q. Kang *et al.*, Selective etching induced synthesis of hollow Rh nanospheres electrocatalyst for alcohol oxidation reactions. *Small* **14**, 1801239 (2018).